Di-electron spectrum at mid-rapidity in $p + p$ collisions at $\sqrt{s} = 200$ GeV

L. Adamczyk,[1] G. Agakishiev,[20] M. M. Aggarwal,[31] Z. Ahammed,[50] A. V. Alakhverdyants,[20] I. Alekseev,[18] J. Alford,[21] B. D. Anderson,[21] C. D. Anson,[29] D. Arkhipkin,[3] E. Aschenauer,[3] G. S. Averichev,[20] J. Balewski,[25] A. Banerjee,[50] Z. Barnovska,[13] D. R. Beavis,[3] R. Bellwied,[46] M. J. Betancourt,[25] R. R. Betts,[9] A. Bhasin,[19] A. K. Bhati,[31] H. Bichsel,[52] J. Bielcik,[12] J. Bielcikova,[13] L. C. Bland,[3] I. G. Bordyuzhin,[18] W. Borowski,[43] J. Bouchet,[21] A. V. Brandin,[28] S. G. Brovko,[5] E. Bruna,[54] S. Bueltmann,[30] I. Bunzarov,[20] T. P. Burton,[3] J. Butterworth,[38] X. Z. Cai,[42] H. Caines,[54] M. Calderón de la Barca Sánchez,[5] D. Cebra,[5] R. Cendejas,[6] M. C. Cervantes,[44] P. Chaloupka,[13] Z. Chang,[44] S. Chattopadhyay,[50] H. F. Chen,[40] J. H. Chen,[42] J. Y. Chen,[8] L. Chen,[8] J. Cheng,[47] M. Cherney,[11] A. Chikanian,[54] W. Christie,[3] P. Chung,[13] J. Chwastowski,[10] M. J. M. Codrington,[44] R. Corliss,[25] J. G. Cramer,[52] H. J. Crawford,[4] X. Cui,[40] A. Davila Leyva,[45] L. C. De Silva,[46] R. R. Debbe,[3] T. G. Dedovich,[20] J. Deng,[41] R. Derradi de Souza,[7] S. Dhamija,[17] L. Didenko,[3] F. Ding,[5] A. Dion,[3] P. Djawotho,[44] X. Dong,[24] J. L. Drachenberg,[44] J. E. Draper,[5] C. M. Du,[23] L. E. Dunkelberger,[6] J. C. Dunlop,[3] L. G. Efimov,[20] M. Elnimr,[53] J. Engelage,[4] G. Eppley,[38] L. Eun,[24] O. Evdokimov,[9] R. Fatemi,[22] S. Fazio,[3] J. Fedorisin,[20] R. G. Fersch,[22] P. Filip,[20] E. Finch,[54] Y. Fisyak,[3] C. A. Gagliardi,[44] D. R. Gangadharan,[29] F. Geurts,[38] A. Gibson,[49] S. Gliske,[2] Y. N. Gorbunov,[11] O. G. Grebenyuk,[24] D. Grosnick,[49] S. Gupta,[19] W. Guryn,[3] B. Haag,[5] O. Hajkova,[12] A. Hamed,[44] L-X. Han,[42] J. W. Harris,[54] J. P. Hays-Wehle,[25] S. Heppelmann,[33] A. Hirsch,[35] G. W. Hoffmann,[45] D. J. Hofman,[9] S. Horvat,[54] B. Huang,[3] H. Z. Huang,[6] P. Huck,[8] T. J. Humanic,[29] L. Huo,[44] G. Igo,[6] W. W. Jacobs,[17] C. Jena,[15] J. Joseph,[21] E. G. Judd,[4] S. Kabana,[43] K. Kang,[47] J. Kapitan,[13] K. Kauder,[9] H. W. Ke,[8] D. Keane,[21] A. Kechechyan,[20] A. Kesich,[5] D. Kettler,[52] D. P. Kikola,[35] J. Kiryluk,[24] A. Kisiel,[51] V. Kizka,[20] S. R. Klein,[24] D. D. Koetke,[49] T. Kollegger,[14] J. Konzer,[35] I. Koralt,[30] L. Koroleva,[18] W. Korsch,[22] L. Kotchenda,[28] P. Kravtsov,[28] K. Krueger,[2] L. Kumar,[21] M. A. C. Lamont,[3] J. M. Landgraf,[3] S. LaPointe,[53] J. Lauret,[3] A. Lebedev,[3] R. Lednicky,[20] J. H. Lee,[3] W. Leight,[25] M. J. LeVine,[3] C. Li,[40] L. Li,[45] W. Li,[42] X. Li,[35] X. Li,[41] Y. Li,[47] Z. M. Li,[8] L. M. Lima,[39] M. A. Lisa,[29] F. Liu,[8] T. Ljubicic,[3] W. J. Llope,[38] R. S. Longacre,[3] Y. Lu,[40] X. Luo,[8] A. Luszczak,[10] G. L. Ma,[42] Y. G. Ma,[42] D. M. M. D. Madagodagettige Don,[11] D. P. Mahapatra,[15] R. Majka,[54] O. I. Mall,[5] S. Margetis,[21] C. Markert,[45] H. Masui,[24] H. S. Matis,[24] D. McDonald,[38] T. S. McShane,[11] S. Mioduszewski,[44] M. K. Mitrovski,[3] Y. Mohammed,[44] B. Mohanty,[50] M. M. Mondal,[44] B. Morozov,[18] M. G. Munhoz,[39] M. K. Mustafa,[35] M. Naglis,[24] B. K. Nandi,[16] Md. Nasim,[50] T. K. Nayak,[50] L. V. Nogach,[34] J. Novak,[27] G. Odyniec,[24] A. Ogawa,[3] K. Oh,[36] A. Ohlson,[54] V. Okorokov,[28] E. W. Oldag,[45] R. A. N. Oliveira,[39] D. Olson,[24] P. Ostrowski,[51] M. Pachr,[12] B. S. Page,[17] S. K. Pal,[50] Y. X. Pan,[6] Y. Pandit,[21] Y. Panebratsev,[20] T. Pawlak,[51] B. Pawlik,[32] H. Pei,[9] C. Perkins,[4] W. Peryt,[51] P. Pile,[3] M. Planinic,[55] J. Pluta,[51] D. Plyku,[30] N. Poljak,[55] J. Porter,[24] A. M. Poskanzer,[24] C. B. Powell,[24] D. Prindle,[52] C. Pruneau,[53] N. K. Pruthi,[31] M. Przybycien,[1] P. R. Pujahari,[16] J. Putschke,[53] H. Qiu,[24] R. Raniwala,[37] S. Raniwala,[37] R. L. Ray,[45] R. Redwine,[25] R. Reed,[5] C. K. Riley,[54] H. G. Ritter,[24] J. B. Roberts,[38] O. V. Rogachevskiy,[20] J. L. Romero,[5] J. F. Ross,[11] L. Ruan,[3] J. Rusnak,[13] N. R. Sahoo,[50] I. Sakrejda,[24] S. Salur,[24] A. Sandacz,[51] J. Sandweiss,[54] E. Sangaline,[5] A. Sarkar,[16] J. Schambach,[45] R. P. Scharenberg,[35] A. M. Schmah,[24] B. Schmidke,[3] N. Schmitz,[26] T. R. Schuster,[14] J. Seele,[25] J. Seger,[11] P. Seyboth,[26] N. Shah,[6] E. Shahaliev,[20] M. Shao,[40] B. Sharma,[31] M. Sharma,[53] S. S. Shi,[8] Q. Y. Shou,[42] E. P. Sichtermann,[24] R. N. Singaraju,[50] M. J. Skoby,[35] D. Smirnov,[3] N. Smirnov,[54] D. Solanki,[37] P. Sorensen,[3] U. G. deSouza,[39] H. M. Spinka,[2] B. Srivastava,[35] T. D. S. Stanislaus,[49] S. G. Steadman,[25] J. R. Stevens,[17] R. Stock,[14] M. Strikhanov,[28] B. Stringfellow,[35] A. A. P. Suaide,[39] M. C. Suarez,[9] M. Sumbera,[13] X. M. Sun,[24] Y. Sun,[40] Z. Sun,[23] B. Surrow,[25] D. N. Svirida,[18] T. J. M. Symons,[24] A. Szanto de Toledo,[39] J. Takahashi,[7] A. H. Tang,[3] Z. Tang,[40] L. H. Tarini,[53] T. Tarnowsky,[27] D. Thein,[45] J. H. Thomas,[24] J. Tian,[42] A. R. Timmins,[46] D. Tlusty,[13] M. Tokarev,[20] T. A. Trainor,[52] S. Trentalange,[6] R. E. Tribble,[44] P. Tribedy,[50] B. A. Trzeciak,[51] O. D. Tsai,[6] J. Turnau,[32] T. Ullrich,[3] D. G. Underwood,[2] G. Van Buren,[3] G. van Nieuwenhuizen,[25] J. A. Vanfossen, Jr.,[21] R. Varma,[16] G. M. S. Vasconcelos,[7] F. Videbæk,[3] Y. P. Viyogi,[50] S. Vokal,[20] S. A. Voloshin,[53] A. Vossen,[17] M. Wada,[45] F. Wang,[35] G. Wang,[6] H. Wang,[27] J. S. Wang,[23] Q. Wang,[35] X. L. Wang,[40] Y. Wang,[47] G. Webb,[22] J. C. Webb,[3] G. D. Westfall,[27] C. Whitten, Jr.,[6,*] H. Wieman,[24] S. W. Wissink,[17] R. Witt,[48] W. Witzke,[22] Y. F. Wu,[8] Z. Xiao,[47] W. Xie,[35] K. Xin,[38] H. Xu,[23] N. Xu,[24] Q. H. Xu,[41] W. Xu,[6] Y. Xu,[40] Z. Xu,[3] L. Xue,[42] Y. Yang,[23] Y. Yang,[8] P. Yepes,[38] Y. Yi,[35] K. Yip,[3] I-K. Yoo,[36] M. Zawisza,[51] H. Zbroszczyk,[51] J. B. Zhang,[8] S. Zhang,[42] W. M. Zhang,[21] X. P. Zhang,[47] Y. Zhang,[40] Z. P. Zhang,[40] F. Zhao,[6] J. Zhao,[42] C. Zhong,[42] X. Zhu,[47] Y. H. Zhu,[42] and Y. Zoulkarneeva[20]

(STAR Collaboration)

[1]*AGH University of Science and Technology, Krakow, Poland*
[2]*Argonne National Laboratory, Argonne, Illinois 60439, USA*
[3]*Brookhaven National Laboratory, Upton, New York 11973, USA*
[4]*University of California, Berkeley, California 94720, USA*
[5]*University of California, Davis, California 95616, USA*
[6]*University of California, Los Angeles, California 90095, USA*
[7]*Universidade Estadual de Campinas, Sao Paulo, Brazil*
[8]*Central China Normal University (HZNU), Wuhan 430079, China*
[9]*University of Illinois at Chicago, Chicago, Illinois 60607, USA*
[10]*Krakow University of Technology, Krakow, Poland*
[11]*Creighton University, Omaha, Nebraska 68178, USA*
[12]*Czech Technical University in Prague, FNSPE, 115 19 Prague, Czech Republic*

[13]*Nuclear Physics Institute AS CR, 250 68 Řež/Prague, Czech Republic*
[14]*University of Frankfurt, Frankfurt, Germany*
[15]*Institute of Physics, Bhubaneswar 751005, India*
[16]*Indian Institute of Technology, Mumbai, India*
[17]*Indiana University, Bloomington, Indiana 47408, USA*
[18]*Alikhanov Institute for Theoretical and Experimental Physics, Moscow, Russia*
[19]*University of Jammu, Jammu 180001, India*
[20]*Joint Institute for Nuclear Research, Dubna 141 980, Russia*
[21]*Kent State University, Kent, Ohio 44242, USA*
[22]*University of Kentucky, Lexington, Kentucky 40506-0055, USA*
[23]*Institute of Modern Physics, Lanzhou, China*
[24]*Lawrence Berkeley National Laboratory, Berkeley, California 94720, USA*
[25]*Massachusetts Institute of Technology, Cambridge, Massachusetts 02139-4307, USA*
[26]*Max-Planck-Institut für Physik, Munich, Germany*
[27]*Michigan State University, East Lansing, Michigan 48824, USA*
[28]*Moscow Engineering Physics Institute, Moscow, Russia*
[29]*Ohio State University, Columbus, Ohio 43210, USA*
[30]*Old Dominion University, Norfolk, Virginia 23529, USA*
[31]*Panjab University, Chandigarh 160014, India*
[32]*Institute of Nuclear Physics PAS, Krakow, Poland*
[33]*Pennsylvania State University, University Park, Pennsylvania 16802, USA*
[34]*Institute of High Energy Physics, Protvino, Russia*
[35]*Purdue University, West Lafayette, Indiana 47907, USA*
[36]*Pusan National University, Pusan, Republic of Korea*
[37]*University of Rajasthan, Jaipur 302004, India*
[38]*Rice University, Houston, Texas 77251, USA*
[39]*Universidade de Sao Paulo, Sao Paulo, Brazil*
[40]*University of Science & Technology of China, Hefei 230026, China*
[41]*Shandong University, Jinan, Shandong 250100, China*
[42]*Shanghai Institute of Applied Physics, Shanghai 201800, China*
[43]*SUBATECH, Nantes, France*
[44]*Texas A&M University, College Station, Texas 77843, USA*
[45]*University of Texas, Austin, Texas 78712, USA*
[46]*University of Houston, Houston, Texas 77204, USA*
[47]*Tsinghua University, Beijing 100084, China*
[48]*United States Naval Academy, Annapolis, Maryland 21402, USA*
[49]*Valparaiso University, Valparaiso, Indiana 46383, USA*
[50]*Variable Energy Cyclotron Centre, Kolkata 700064, India*
[51]*Warsaw University of Technology, Warsaw, Poland*
[52]*University of Washington, Seattle, Washington 98195, USA*
[53]*Wayne State University, Detroit, Michigan 48201, USA*
[54]*Yale University, New Haven, Connecticut 06520, USA*
[55]*University of Zagreb, HR-10002 Zagreb, Croatia*
(Received 9 April 2012; published 8 August 2012)

We report on the mid-rapidity mass spectrum of di-electrons and cross sections of pseudoscalar and vector mesons via e^+e^- decays, from $\sqrt{s} = 200$ GeV $p + p$ collisions, measured by the large-acceptance experiment STAR at the Relativistic Heavy Ion Collider. The ratio of the di-electron continuum to the combinatorial background is larger than 10% over the entire mass range. Simulations of di-electrons from light-meson decays and heavy-flavor decays (charmonium and open charm correlation) are found to describe the data. The extracted $\omega \to e^+e^-$ invariant yields are consistent with previous measurements. The mid-rapidity yields (dN/dy) of ϕ and J/ψ are extracted through their di-electron decay channels and are consistent with the previous measurements of $\phi \to K^+K^-$ and $J/\psi \to e^+e^-$. Our results suggest a new upper limit of the branching ratio of the $\eta \to e^+e^-$ of 1.7×10^{-5} at the 90% confidence level.

DOI: 10.1103/PhysRevC.86.024906 PACS number(s): 25.75.Dw

I. INTRODUCTION

Dileptons are a crucial probe of the strongly interacting matter created in ultrarelativistic heavy-ion collisions [1,2]. Leptons are produced during the whole evolution of the created matter and can traverse the medium with minimal interactions. Different kinematics of dilepton pairs (mass and transverse momentum ranges) can selectively probe the properties of the formed matter throughout its entire evolution [3,4].

In the low-invariant-mass range of produced lepton pairs ($M_{ll} < 1.1$ GeV/c^2), vector meson in-medium properties [mass and width of the spectral functions of $\rho(770)$, $\omega(782)$, and $\phi(1020)$] may be studied via dilepton decays and may exhibit modifications related to possible chiral symmetry restoration [3,4]. For example, at the Super Proton Synchrotron (SPS), an explanation of the low-mass dilepton enhancement in the CERES e^+e^- data from Pb + Au collisions requires substantial medium effects on the ρ-meson spectral function [5]. Also, NA60 recently reported a significant excess of low-mass $\mu^+\mu^-$ pairs in In + In collisions above the yield expected from neutral meson decays [6], which is consistent with a broadened spectral function [7] but not a dropping-mass scenario [8].

At the Relativistic Heavy Ion Collider (RHIC), the PHENIX experiment observed a significant enhancement for $0.15 < M_{ee} < 0.75$ GeV/c^2 in the low-transverse-momentum ($p_T <$ 1 GeV/c) part of the di-electron continuum in Au + Au collisions compared to that expected from hadronic sources [9]. Models that successfully describe the SPS dilepton data consistently fail to describe the PHENIX data in the low-mass and low-p_T region [9,10]. Also, in the higher p_T range, direct photon yields were derived through di-electron measurements at RHIC, allowing an assessment of thermal radiation [11]. Additional precision experiments with large acceptance and a broad range of beam energies can provide invaluable insights into this subject [1].

The dilepton spectra in the intermediate mass range ($1.1 < M_{ll} < 3.0$ GeV/c^2) are expected to be directly related to the thermal radiation of the quark-gluon plasma (QGP) [3,4]. However, significant background contributions from other sources have to be measured experimentally. Such contributions include background pairs from correlated open heavy-flavor decays, which produce a pair of electrons or muons from the semileptonic decay of a pair of open charm or bottom hadrons ($c\bar{c} \to l^+l^-$ or $b\bar{b} \to l^+l^-$). In the high-mass region ($M_{ll} > 3.0$ GeV/c^2), J/ψ, Υ, and their excited states are used to study the color-screening features of the QGP [12]. The PHENIX Collaboration has a reported di-electron spectrum in $p+p$ collisions and has found the data to be very well described by the hadronic cocktail and heavy flavor decays for the entire mass range within the uncertainty of the data and the cocktail [9]. The first di-electron continuum measurement from STAR in $\sqrt{s} = 200$ GeV $p+p$ collisions, presented in this paper, provides a crucial reference for corresponding future STAR measurements in heavy-ion collisions.

Rare processes such as leptonic decays of hadrons provide possible observables to be used in searching for traces of new physics beyond the Standard Model (BSM) [13–16]. These decays usually involve electromagnetic or weak couplings which can be calculated to a high degree of accuracy within the Standard Model (SM). In addition to a direct observation of the Higgs boson, the Large Hadron Collider (LHC) looks to explore BSM physics. Deviations of rare process observables from SM predictions may be taken as indirect evidence of a new coupling beyond the SM physics [13], which can also be explored at lower energies. The pseudoscalar mesons (for example, η or η') are particularly interesting since their decay to e^+e^- pairs is suppressed by $\alpha^2(10^{-4})$ and by helicity conservation due to the small electron mass [$r^2 = (m_e/m_\eta)^2 \simeq 10^{-6}$] [17]. The branching ratio (B.R.) of $\eta \to e^+e^-$ is 2.3×10^{-9} according to the SM predictions; however, couplings from BSM physics may increase this B.R. significantly [13]. RHIC offers high-luminosity nucleus-nucleus collisions with large multiplicities and copious hadrons of interest, thereby providing a unique environment for studying rare decay processes, nuclear medium effects, and searching for BSM physics. With recent upgrades, including the new time-of-flight detector (TOF) [18] and improved data acquisition system [19], the STAR experiment is able to benefit from a high rate capability as well as excellent lepton identification at low momentum in the search for rare decays.

This paper is organized as follows. Section II shows the detector and data sample used in this analysis. Section III describes the analysis details including electron identification, electron-pair distributions, background subtraction, and di-electron continuum without efficiency correction. Section IV presents the details of the simulations of di-electrons from light-meson decays and heavy-flavor decays, collectively called cocktail simulations. The efficiency correction for the di-electron continuum, the corrected di-electron continuum, and systematic uncertainties are also discussed in this section. Results on the yields of ω, ϕ, and J/ψ from di-electronic decays are presented in detail in Sec. V. The rare decay of $\eta \to e^+e^-$ is discussed in Sec. VI. Lastly, Sec. VII provides a concluding summary.

II. DETECTORS AND DATA SAMPLE

Two subdetectors are used in this analysis at mid-rapidity at STAR [20]: the time projection chamber (TPC) [21] and a newly installed TOF [18]. The TPC is the main tracking detector at STAR, measuring momenta, charge, and energy loss of charged particles. The TPC, immersed in a 0.5-T solenoidal magnetic field, is a 4.2-m-long cylinder surrounding the beam pipe. Its fiducial volume ranges from 50 to 200 cm radially and is filled with P10 gas (90% argon and 10% methane). Electrons from ionized gas drift toward the nearest end cap, where the signals are read out. The TPC readout is divided azimuthally into 24 sectors, 12 at each end. Each sector is divided into inner and outer subsectors with a total of 45 pad row readouts. The pad row readouts provide precise positions of primary ionization clusters (hits) generated by charged particles. The ionization energy loss of a charged particle in the TPC gas (dE/dx) is used for particle identification [22,23]. The most probable dE/dx is determined from the mean of

*Deceased.

a distribution in which the 30% of clusters with the largest signals are discarded (i.e., a truncated mean). For the data taken in 2009 and analyzed here, 72% of the full TOF system was installed and operational. The full TOF system contains 120 units, which we call trays, 60 in the pseudo-rapidity range $0<\eta<0.9$ and 60 for $-0.9<\eta<0$, with each tray covering 6° in azimuth. The TOF has a typical stop timing resolution of 85 ps, allowing the identification of $\pi(K)$ up to a momentum of 1.6 GeV/c and $p(\bar{p})$ up to a momentum of 3 GeV/c [24,25].

The minimum-bias triggered events were defined by the coincidence of signals in the two vertex position detectors (VPDs) [26], located on each side of the STAR interaction region and covering $4.4<|\eta|<4.9$. This di-electron analysis used 107 million minimally biased events from non-singly diffractive (NSD) $\sqrt{s}=200$ GeV $p+p$ collisions ($\sigma_{\rm NSD}=30.0\pm3.5$ mb [27]), in which the collision vertex is required to be within 50 cm of the mean of the distribution, nominally at the center of the TPC and along the beam line.

III. DATA ANALYSIS

A. Tracking and particle identification

Hits belonging to charged particles traversing the TPC are collected and reconstructed into tracks with well-defined geometry, momentum (p), and dE/dx. Only tracks that project back to within 1 cm of the collision vertex are retained in the analysis, thereby limiting the combinatorial background from conversions and enabling a high detecting efficiency. The tracks are required to have at least 25 hits out of a maximum of 45 to avoid split tracks. Also, a minimum of 15 hits is required in the dE/dx measurement to obtain good dE/dx resolution [21,28]. For particles directly originating from the collision, the collision vertex is added as an additional hit to further improve the momentum measurement [28].

Figure 1(a) shows the $1/\beta$ of particles versus momentum from the TOF in $p+p$ collisions while Figs. 1(b) and 1(c) show the normalized dE/dx ($n\sigma_e$) distribution from the TPC as a function of p_T, without and with a requirement of high velocity $|1/\beta-1|<0.03$, respectively. The quantity $n\sigma_e$ is defined as $n\sigma_e=\ln(\frac{dE}{dx}/I_e)/R_e$, where dE/dx is the measured specific energy loss of a particle and I_e is the expected dE/dx of an electron. R_e is the $\ln(\frac{dE}{dx}/I_e)$ resolution of an electron and is better than 8%. Electron candidates whose $n\sigma_e$ falls between the lines indicated in Fig. 1(c) are retained in this analysis. With a perfect calibration, $n\sigma_e$ for single electrons should follow a standard normal distribution. Figure 2 shows the $n\sigma_e$ distribution for $0.4<p_T<0.5$ GeV/c after the cut of $|1/\beta-1|<0.03$. The two dashed lines perpendicular to the x axis represent the range of the $n\sigma_e$ cut in this p_T region. A Gaussian plus exponential function, respectively representing the electron and hadron components, is used to fit the $n\sigma_e$ distribution. From the fit, we derive the purity and the $n\sigma_e$ cut efficiency on electron candidates as a function of p_T, as shown in Fig. 3. The purity is defined within a range of $n\sigma_e$ (i.e., between the vertical dashed lines in Fig. 2) as being the ratio of the electron counts in the area of the dashed Gaussian to the counts of all particles. The efficiency is defined to be the ratio of the electron counts under the dashed Gaussian within a range of

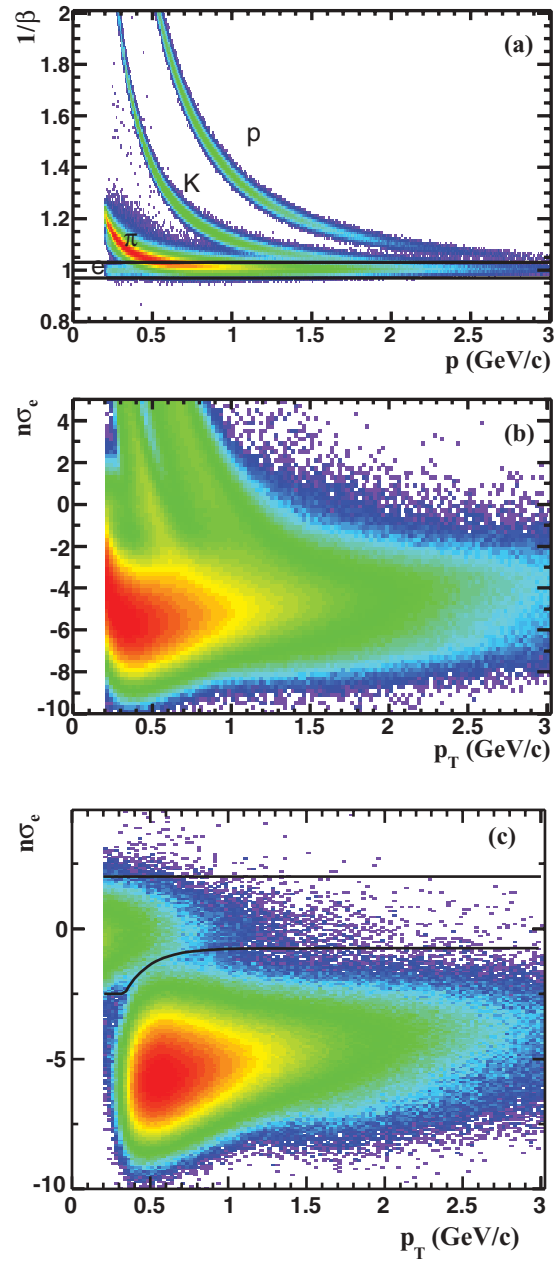

FIG. 1. (Color online) (a) $1/\beta$ vs momentum of tracks from the TOF with $|\eta|<1$ from 200-GeV $p+p$ collisions. The line indicates the cut of $|1/\beta-1|<0.03$. (b) The normalized dE/dx distribution from the TPC as a function of p_T. (c) The normalized dE/dx distribution from the TPC as a function of p_T with the cut of $|1/\beta-1|<0.03$. An electron band, indicated by the lines, is prominent, with the requirement of velocity close to the speed of light from the TOF measurement.

$n\sigma_e$ to the total electron counts under the dashed Gaussian. The errors on the efficiency and purity are determined by adjusting the fit range. The electron yields are sensitive to the fit range since the hadron contamination increases in the smaller $n\sigma_e$ region, thereby leading to large errors for the efficiency for $p_T>0.8$ GeV/c. Our exponential extrapolation of the $n\sigma_e$ distribution for the hadron component tends to overestimate the background and therefore should be taken as an upper

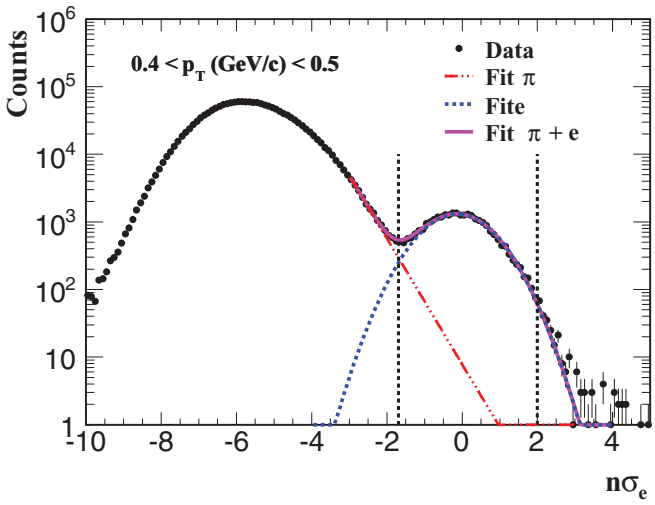

FIG. 2. (Color online) The $n\sigma_e$ distribution in $0.4 < p_T < 0.5$ GeV/c after the cut of $|1/\beta - 1| < 0.03$ is applied. The solid curve represents a Gaussian plus exponential fit to the $n\sigma_e$ distribution. The dot-dashed line is for the hadron component and the dashed line is for the electron contribution. The two dashed lines perpendicular to the x axis represent the range of the $n\sigma_e$ cut to ensure a high purity for electron candidates in this p_T range.

limit on the hadron contamination. By combining the velocity (β) information from the TOF and the dE/dx from the TPC, electrons can be clearly identified from low to intermediate p_T ($p_T < 3$ GeV/c) for $|\eta| < 1$ [29].

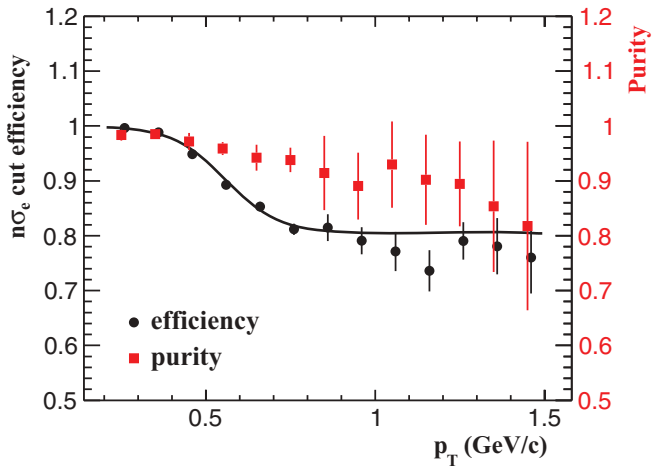

FIG. 3. (Color online) The purity and the $n\sigma_e$ cut efficiency for electron candidates as a function of p_T in $|\eta| < 1$ for $p + p$ collisions at $\sqrt{s} = 200$ GeV. The squares represent the purity and closed circles represent the $n\sigma_e$ efficiency. The p_T positions of the last three data points for the efficiency are slightly shifted for clarity. The error bars are the quadrature sum of statistical and systematic uncertainties. A function form of $A + B/[C + \exp(D \times p_T)]$ is used to fit the efficiency data points and for the efficiency correction, in which A, B, C, and D are the fit parameters. A constant component in the fit for $p_T > 0.8$ GeV/c is driven by the study in Ref. [23].

B. Di-electron invariant-mass distribution and background subtraction

With a high purity for the electron samples, the e^+ and e^- from the same events are combined to generate the invariant-mass distributions (M_{ee}) of e^+e^- pairs called unlike-sign distributions. The unlike-sign distributions contain both signal and background. The signals are di-electrons from light-meson decays and heavy-flavor decays (charmonium and open charm correlation). The background results from random combinatorial pairs and correlated pairs. Electron candidates are required to be in the range of $|\eta| < 1$ and $p_T > 0.2$ GeV/c while e^+e^- pairs are required to be in the rapidity range of $|y_{ee}| < 1$.

The following two techniques are used for background estimation. In the like-sign technique, electron pairs with the same charge sign are combined from the same events. In the mixed-event technique, unlike-sign pairs are formed from different events. In order to ensure the events used in mixing have similar geometric acceptance in the detector, we only mix events which have collision vertices within 5 cm of each other along the beam line direction.

Neither method represents the background perfectly. In the low-mass region, there is a correlated cross-pair background (coming from two pairs of e^+e^- from the same meson decays: Dalitz decays followed by a conversion of the decay photon or conversions of multiple photons from the same meson). This background is present in the like-sign distribution but not in the mixed-event background. On the other hand, due to the sector structure of detectors and the different curvatures of positively and negatively charged particle tracks in the plane perpendicular to the magnetic field, like-sign and unlike-sign pairs will have different acceptance. Moreover, in the high-invariant-mass range, there may be contributions from jet correlations which are absent from the mixed-event technique.

Figure 4 shows the invariant-mass distribution for unlike-sign pairs, like-sign pairs, and mixed-event background. The mixed-event distribution is normalized by a constant to match the like-sign distribution in the mass range 0.4–1.5 GeV/c^2. In our analysis we subtract the like-sign background for $M_{ee} <$ 0.4 GeV/c^2 and the mixed-event background in the higher mass region.

For a cross-check on the consistency of the two methods we compare their shapes in the higher mass region (Fig. 5). A constant fits the ratio of like-sign over mixed-event distributions for $M_{ee} > 0.4$ GeV/c^2 with $\chi^2/\text{NDF} = 14/15$, where NDF is the number of degrees of freedom, as shown in the ratio plot in Fig. 5(a). We also find that for electron pairs with significantly higher transverse momentum (as determined from the Barrel Electro-Magnetic Calorimeter triggered events), the shapes of like-sign and mixed-event distributions agree in the mass region of 1–3 GeV/c^2 [30]. Figure 5(b) shows the distribution of the difference of the azimuthal angles ($\Delta\phi$) of the two electrons in the unlike-sign, like-sign, and mixed-event pairs. The difference between like-sign and mixed-event pairs at low $\Delta\phi$ can be attributed to cross-pair contributions. For $M_{ee} > 0.4$ GeV/c^2, the $\Delta\phi$ distributions of like-sign and mixed-event pairs match nicely with each other, as shown in Fig. 5(c), indicating that mixed-event background subtraction is valid in the corresponding mass region.

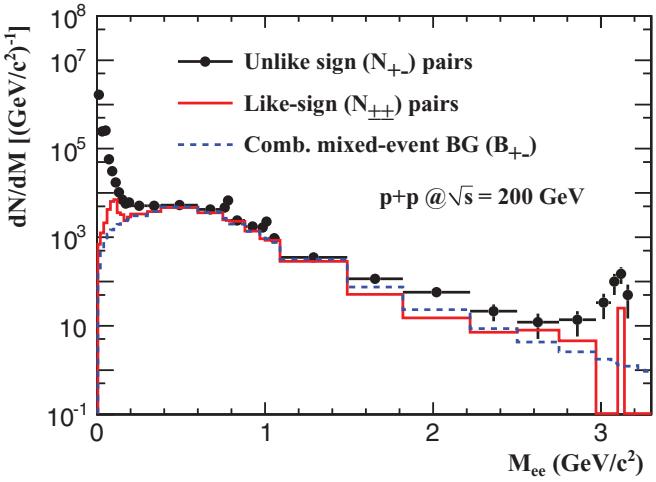

FIG. 4. (Color online) The electron-pair invariant-mass distributions for unlike-sign pairs, like-sign pairs, and mixed-event (combinatorial) background in minimum-bias $p+p$ collisions. The electron candidates are required to be in the range of $|\eta|<1$ and have a p_T value greater than 0.2 GeV/c. The ee pairs were required to be in the rapidity range of $|y_{ee}|<1$. The uneven bin widths are used based on the yields and the signal-to-background ratios.

As an additional check with a different method, we also perform the analysis by subtracting the like-sign background in the whole mass region. The difference in the di-electron yields from the mixed-event and like-sign methods is found to be within errors for $M_{ee}>0.4$ GeV/c^2. We also correct for acceptance differences between the like-sign and unlike-sign electron pairs in both methods and will discuss the details in Sec. IV C.

Figure 6(a) shows the di-electron continuum after background subtraction from both like-sign and mixed-event methods in $p+p$ collisions at $\sqrt{s}=200$ GeV. The measurements are done by requiring $|y_{e^+e^-}|<1$, $|\eta_e|<1$, and $p_T(e)>0.2$ GeV/c and no efficiency correction has been applied. The two methods give consistent results for $M_{ee}>0.4$ GeV/c^2. For the following, we use the yields from the like-sign method for $M_{ee}<0.4$ GeV/c^2 and results obtained from the mixed-event method at higher mass as the default since the mixed-event background distribution matches the like-sign distribution and has better precision for $M_{ee}>0.4$ GeV/c^2. The signal-to-background ratio in $p+p$ collisions versus M_{ee} is shown in Fig. 6(b).

IV. DI-ELECTRON CONTINUUM IN STAR ACCEPTANCE

A. Cocktail simulation

The di-electron pairs may come from decays of the light-flavor and heavy-flavor hadrons. They include π^0, η, and η' Dalitz decays: $\pi^0\to\gamma e^+e^-$, $\eta\to\gamma e^+e^-$, and $\eta'\to\gamma e^+e^-$; vector meson decays: $\omega\to\pi^0e^+e^-$, $\omega\to e^+e^-$, $\rho^0\to e^+e^-$, $\phi\to\eta e^+e^-$, $\phi\to e^+e^-$, and $J/\psi\to e^+e^-$; heavy-flavor hadron semileptonic decays: $c\bar{c}\to e^+e^-$ and $b\bar{b}\to e^+e^-$; and Drell-Yan contributions. We fit the invariant yields of mesons, previously measured at STAR and PHENIX as discussed below, with the Tsallis functions [31], as shown in Fig. 7(a). We use the Tsallis functions as input to a detector simulation in which the particles are decayed into di-electrons with the appropriate branching ratios. This GEANT detector simulation [32] uses a detailed description of the STAR geometry in 2009. Simulated e^+e^- cocktails from the various contributing sources, as shown in Fig. 7(b), are selected using the same cut conditions as those in the analyses of real events. The di-electron contributions from the γ conversion $\gamma\to e^+e^-$ in the detector material are accepted in both data and simulation subject to the same analysis cuts as well. The imperfect description of the material in the simulation leads to 3% systematic uncertainty for the cocktail simulation for $M_{ee}<0.1$ GeV/c^2. The Dalitz decays of $\eta\to\gamma^0e^+e^-$, $\omega\to\pi^0e^+e^-$, and $\eta'\to\gamma e^+e^-$ are obtained using the Kroll-Wada expression [33].

For the Dalitz decays of π^0, η, and η', we use the formula

$$\frac{dN}{dM_{ee}}\propto\sqrt{1-\frac{4m_e^2}{M_{ee}^2}}\left(1+\frac{2m_e^2}{M_{ee}^2}\right)\frac{1}{M_{ee}}\times\left(1-\frac{M_{ee}^2}{M_h^2}\right)^3\left|F\left(M_{ee}^2\right)\right|^2, \quad (1)$$

in which m_e is the electron mass, M_{ee} is the di-electron mass, and M_h is the mass of the hadron which decays into the di-electron. $F(M_{ee}^2)$ is the electromagnetic transition form factor. For the Dalitz decays of vector mesons ω and ϕ ($A\to Be^+e^-$),

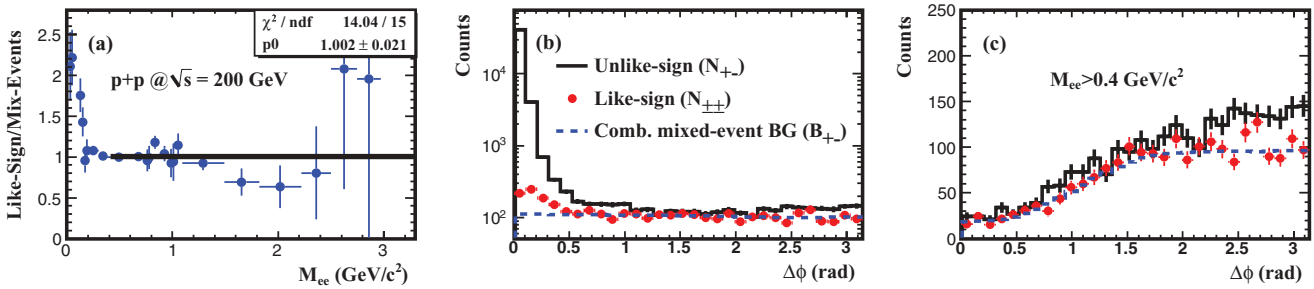

FIG. 5. (Color online) (a) The ratio of like-sign to mixed-event distributions in minimum-bias $p+p$ collisions. (b) The distribution of the difference of the azimuthal angles ($\Delta\phi$) of the two electrons in the unlike-sign, like-sign, and mixed-event pairs in minimum-bias $p+p$ collisions. (c) The $\Delta\phi$ distributions of unlike-sign, like-sign, and mixed-event pairs for $M_{ee}>0.4$ GeV/c^2 in minimum-bias $p+p$ collisions. Errors are statistical.

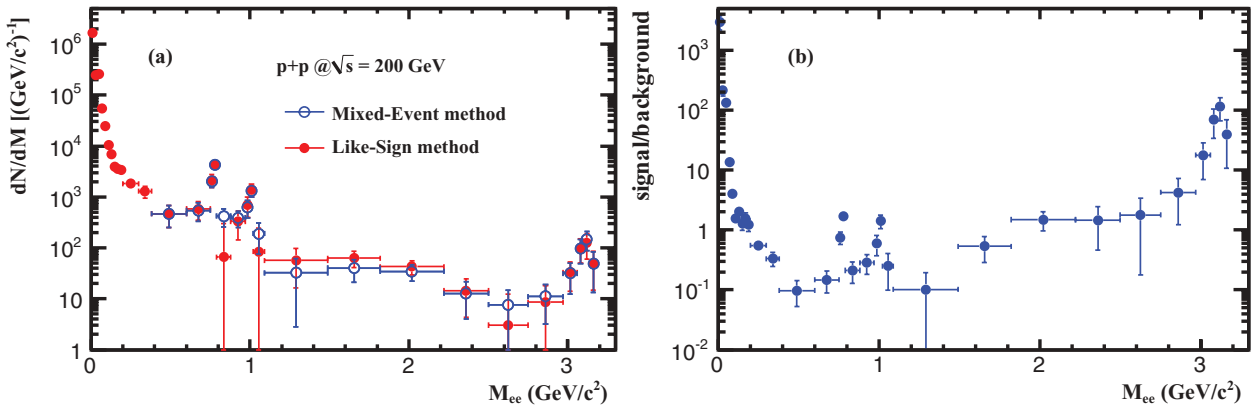

FIG. 6. (Color online) (a) The di-electron (e^+e^-) continuum after background subtraction without efficiency correction in $\sqrt{s} = 200$ GeV minimum-bias $p + p$ collisions. Two methods of obtaining the background are indicated. Errors are statistical only. (b) The signal over background ratio, plotted as a function of M_{ee} for NSD $p + p$ collisions at $\sqrt{s} = 200$ GeV. Errors are statistical.

the formula is

$$\frac{dN}{dM_{ee}} \propto \sqrt{1-\frac{4m_e^2}{M_{ee}^2}}\left(1+\frac{2m_e^2}{M_{ee}^2}\right)\frac{1}{M_{ee}}\left[\left(1+\frac{M_{ee}^2}{M_A^2-M_B^2}\right)^2 - \frac{4M_A^2M_{ee}^2}{\left(M_A^2-M_B^2\right)^2}\right]^{3/2}\left|F\left(M_{ee}^2\right)\right|^2, \quad (2)$$

in which M_A and M_B are the masses of particles A and B, respectively. For all Dalitz decays except η', the form factor is parameterized as

$$F\left(M_{ee}^2\right) = \frac{1}{1-M_{ee}^2\Lambda^{-2}}, \quad (3)$$

in which Λ^{-2} is the form factor slope. For η', we use the parametrization from Ref. [17]:

$$\left|F\left(M_{ee}^2\right)\right|^2 = \frac{1}{\left(1-M_{ee}^2\Lambda^{-2}\right)^2+\Gamma_0^2\Lambda^{-2}}, \quad (4)$$

where Γ_0^2 is 1.99×10^{-2} $(\mathrm{GeV}/c^2)^2$. The Λ parameters are listed in Table I.

The $\rho^0 \to e^+e^-$ line shape is convoluted with the Boltzmann phase space factor [34,35] and given by

$$\frac{dN}{dM_{ee}dp_T} \propto \frac{M_{ee}M_\rho\Gamma_{ee}}{\left(M_\rho^2-M_{ee}^2\right)^2+M_\rho^2(\Gamma_{\pi\pi}+\Gamma_{ee}\Gamma_2)^2}\mathrm{PS}, \quad (5)$$

$$\Gamma_{\pi\pi} = \Gamma_0\frac{M_\rho}{M_{ee}}\left(\frac{M_{ee}^2-4M_\pi^2}{M_\rho^2-4M_\pi^2}\right)^{3/2}, \quad (6)$$

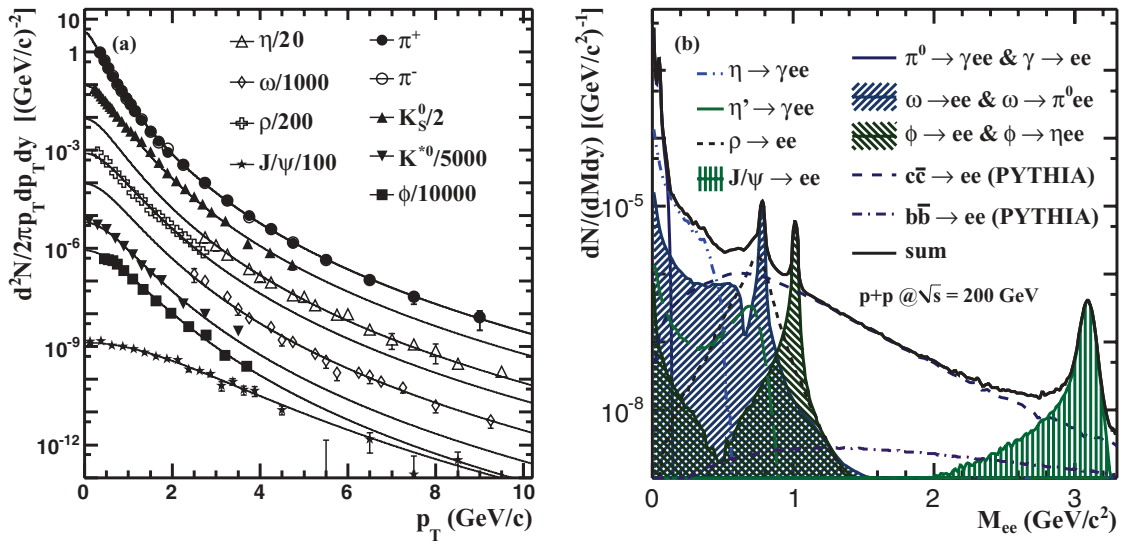

FIG. 7. (Color online) (a) The invariant yields of measured mesons fit with the Tsallis functions [31] in $p + p$ collisions at $\sqrt{s} = 200$ GeV. See text for details. (b) The simulated raw di-electron continuum within STAR acceptance for $\sqrt{s} = 200$ GeV minimum-bias $p + p$ collisions. Different cocktail contributions are shown.

TABLE I. The total yields at mid-rapidity (dN/dy) from the Tsallis fit, decay branching ratios, and Λ parameters of hadrons in NSD $p+p$ collisions at $\sqrt{s}=200$ GeV.

Meson	$\frac{dN}{dy}$	Relative uncertainty	Decay channel	B.R.	Λ^{-2} $(\mathrm{GeV}/c^2)^{-2}$
π^0	1.28	14%	γe^+e^-	1.174×10^{-2}	1.756 ± 0.022 [36]
η	1.7×10^{-1}	23%	γe^+e^-	7.0×10^{-3}	1.95 ± 0.18 [37]
ρ	2.2×10^{-1}	15%	e^+e^-	4.72×10^{-5}	–
ω	1.3×10^{-1}	21%	e^+e^-	7.28×10^{-5}	–
ω			$\pi^0e^+e^-$	7.7×10^{-4}	2.24 ± 0.06 [37]
ϕ	1.7×10^{-2}	20%	e^+e^-	2.954×10^{-4}	–
ϕ			ηe^+e^-	1.15×10^{-4}	3.8 ± 1.8 [38]
η'	4.1×10^{-2}	29%	γe^+e^-	4.7×10^{-4} [39]	1.8 ± 0.4 [17]
J/ψ	2.4×10^{-5}	15%	e^+e^-	5.94×10^{-2}	–

$$\Gamma_{ee}=\Gamma_0\frac{M_\rho}{M_{ee}}\left(\frac{M_{ee}^2-4m_e^2}{M_\rho^2-4m_e^2}\right)^{1/2}, \tag{7}$$

$$PS=\frac{M_{ee}}{\sqrt{M_{ee}^2+p_T^2}}\exp\left(-\frac{\sqrt{M_{ee}^2+p_T^2}}{T}\right), \tag{8}$$

where M_ρ is 776 MeV/c^2, M_π is the π mass, Γ_0 is 149 MeV/c^2, Γ_2 is the B.R. of $\rho^0\to e^+e^-$, PS is the Boltzmann phase space factor, and the inverse slope parameter T is 160 MeV [34]. We neglect any contribution from the interference effect [40] between ρ^0 and ω.

The invariant yield of π^0 is taken as the average of π^+ and π^- [25,41]. The yields of ϕ [42] and ρ^0 [35] are from STAR while the η [43], ω [44], and J/ψ [45] yields are measurements by PHENIX. Table I lists the total yields at mid-rapidity ($dN/dy|_{y=0}$) in 200-GeV NSD $p+p$ collisions.

The last input we consider in the cocktail simulation is the $c\bar{c}$ cross section, which has been constrained by the published low-p_T D^0 spectrum in 200-GeV $d+$Au collisions [29], the nonphotonic electron spectrum in 200-GeV $p+p$ collisions [46], and the di-electron continuum in this analysis. The details of these constraints will be shown in Sec. IV C. The e^+e^- shapes from open heavy-flavor pairs are obtained using PYTHIA6.416, in which the k_T factor is set by PARP(91) = 1 GeV/c, and the parton shower is set by PARP(67) = 1 [47]. With these parameters chosen, PYTHIA can describe the shape of the STAR measured D^0 spectrum and the nonphotonic electron spectrum. The total contribution from the simulation is shown as the black solid curve in Fig. 7(b). In the intermediate-mass region, the di-electron continuum is dominated by the $c\bar{c}$ contribution.

B. Efficiency and acceptance correction

For the di-electron continuum, the efficiency corrections are applied within the STAR acceptance of $|y_{e^+e^-}|<1$, $|\eta_e|<1$, and $p_T(e)>0.2$ GeV/c. The single-electron efficiency includes the TPC tracking efficiency, TOF acceptance and detector response, and the dE/dx efficiency. Single-electron tracking efficiency and acceptance in the TPC are determined by Monte Carlo GEANT simulations. The TOF acceptance and response efficiency for electrons is found to be 46%, independent of p_T for $|\eta|<1$ [25]. The efficiency of the $n\sigma_e$ cut, used to ensure a high purity for the electron sample, is close to 100% at low p_T and falls to ~80% by $p_T=0.8$ GeV/c, as shown in Fig. 3.

Figure 8 shows the efficiency for single electrons in the pseudo-rapidity range of $|\eta|<1$ in $p+p$ collisions at $\sqrt{s}=200$ GeV. Open circles represent the TPC tracking efficiency alone. Including TOF matching and response decreases the efficiency, as shown by the triangles. With additional dE/dx cuts, the final efficiency for single electrons for $|\eta_e|<1$ is shown as squares. For this analysis, 86 out of a possible 120 total TOF trays were installed and the efficiency dependence on azimuthal angle is shown in Fig. 9 for positive and negative η regions. We have accounted for the incomplete TOF acceptance in determining efficiencies for the di-electron spectra.

The efficiency factor for the di-electron continuum within STAR's acceptance is obtained in two steps. We obtain the

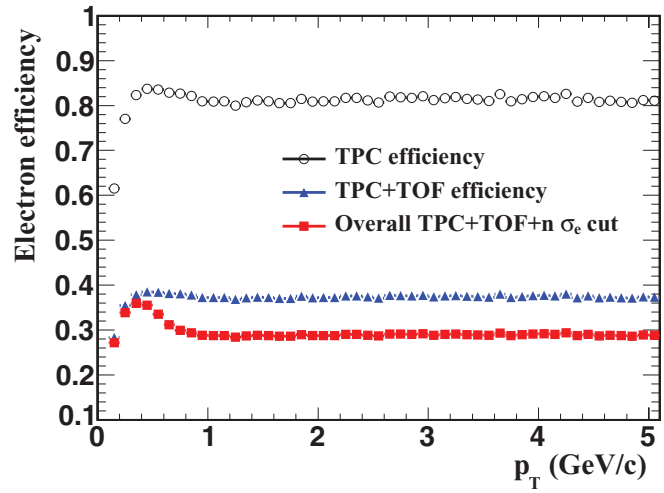

FIG. 8. (Color online) The efficiency for single electrons as a function of p_T in the pseudo-rapidity range of $|\eta|<1$ from $p+p$ collisions at $\sqrt{s}=200$ GeV. Open circles represent the TPC tracking efficiency. With additional TOF matching and response, the efficiency is shown as triangles. With additional dE/dx cuts, the final efficiency is shown as squares.

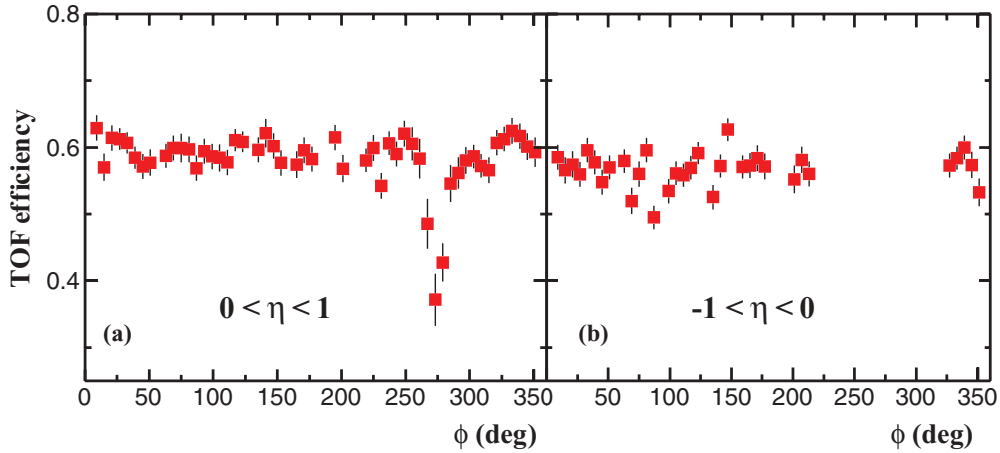

FIG. 9. (Color online) The TOF efficiency as a function of azimuthal angle in the positive and negative η regions. The hole in the negative η region corresponds to the trays (28%) missing from the 2009 run installation. The three trays around 270° in the positive η region have smaller matching efficiencies but have similar performances in other aspects.

input cocktail A within STAR acceptance by the method described in Sec. IV A. The input cocktail includes the radiation energy loss and momentum resolution determined from GEANT simulations. The result is shown by the solid line in Fig. 10(a). Then we obtain cocktail B from GEANT simulations with proper efficiency factors including the TPC tracking, TOF acceptance and response, and dE/dx cut for single electrons as described above and shown as the dashed line in Fig. 10(a). The ratio of these two is the efficiency factor for the di-electrons shown in Fig. 10(b) for $p + p$ collisions at $\sqrt{s} = 200$ GeV. The uncertainty on the efficiency factor is about 10% with a negligible p_T dependence. The final di-electron continuum within the STAR acceptance is obtained after this correction is applied and is discussed in Sec. IV C.

C. Results

The systematic uncertainties on the di-electron continuum are dominated by background subtraction (acceptance difference between like-sign and unlike-sign electron pairs and normalization of mixed-event distributions) and hadron contamination. The acceptances of the like-sign and unlike-sign distributions are the same within 5% for $M_{ee} > 0.1$ GeV/c^2 due to the azimuthal symmetry and the solenoidal magnetic field. The small acceptance differences due to track merging, sector boundaries, and dead channels have been evaluated using the differences of the unlike-sign and like-sign distributions from the mixed-event technique. This difference is included in the systematic uncertainty. In addition, for $M_{ee} > 0.4$ GeV/c^2, the normalization factor between the mixed-event and the like-sign distributions contributes 0%–7% to the overall uncertainty. The systematic uncertainty from efficiency factors is about 10% with no significant mass dependence. The uncertainties in hadron contamination (hadrons from resonance decays misidentified as electrons) are 0%–32% and are mass dependent. Figure 11 shows the relative systematic uncertainties from different sources for each mass bin. The normalization uncertainty in NSD $p + p$ collisions is 8% [46]. Additional contribution from the normalization uncertainty in VPD triggered minimum-bias events taking into account the trigger bias and vertex finding efficiency is 8% as determined from PYTHIA simulations. The total normalization uncertainty

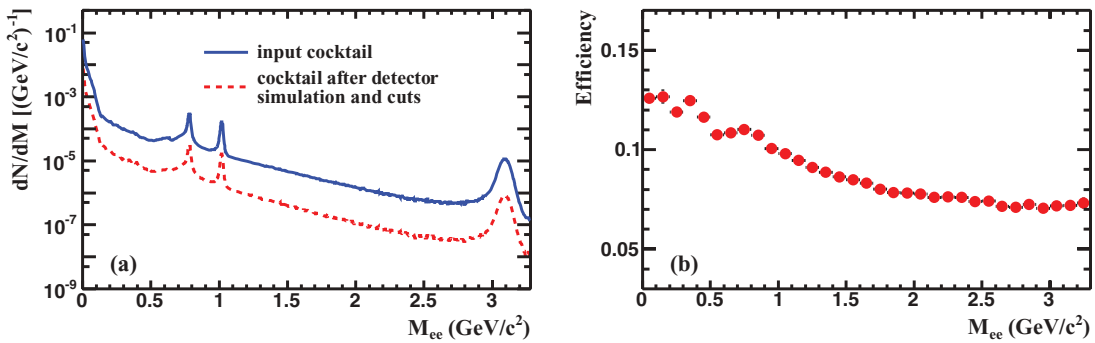

FIG. 10. (Color online) (a) The M_{ee} distribution within STAR's acceptance ($|y_{e^+e^-}| < 1$, $|\eta_e| < 1$, and $p_T(e) > 0.2$ GeV/c) from simulation. The solid line represents the input cocktail. The dashed line represents the cocktail from GEANT simulations taking into account the proper efficiency factors described in the text. (b) The efficiency of the di-electron continuum as a function of M_{ee} within the STAR acceptance in $p + p$ collisions at $\sqrt{s} = 200$ GeV.

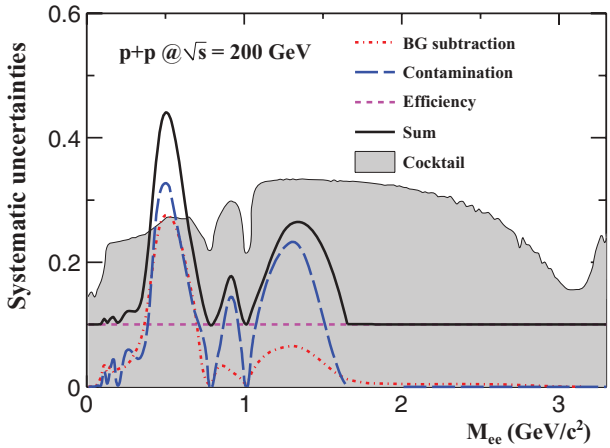

FIG. 11. (Color online) Systematic uncertainties as a function of mass from different source contributions. Also shown are the systematic uncertainties of the cocktail simulation.

for di-electron mass spectra is 11% in $p+p$ collisions. Table II shows the systematic uncertainties from different sources.

The uncertainties on the cocktail simulations include the decay form factors and the measured cross section for each hadron. By fitting the di-electron continuum, open charm [29], and nonphotonic electron spectra [46] simultaneously, we find that the $c\bar{c}$ cross section in 200-GeV $p+p$ collisions is $0.92 \pm 0.10 \pm 0.26$ mb, consistent with earlier RHIC measurements [29,48]. This value is used to generate the charm component in this paper. The systematic uncertainties for the cocktail simulation as a function of mass are shown in Fig. 11. Future precise measurements of the di-electron continuum in the intermediate-mass region can further constrain the charm production mechanism in $p+p$ collisions.

After the efficiency correction, the di-electron continuum within the STAR acceptance is shown in Fig. 12 for $\sqrt{s} = 200$ GeV NSD $p+p$ collisions. The di-electron mass spectrum is not corrected for momentum resolution and radiation energy loss effects. The ratio of data to cocktail simulation is shown in the lower panel of Fig. 12. Within the uncertainties, the cocktail simulation is consistent with the measured di-electron continuum. The χ^2/NDF values between data and cocktail simulation are 21/26 for $M_{ee} > 0.1$ GeV/c^2 and 8/7 for $1.1 < M_{ee} < 3.0$ GeV/c^2. In the mass region $0.2 < M_{ee} < 0.8$ GeV/c^2, the cocktail simulation is systematically higher than the measured di-electron continuum. However,

TABLE II. Systematic uncertainties from different sources for the di-electron continuum.

Source	Contribution factors
background subtraction	0%–27%
contamination	0%–32%
efficiency	10%
total normalization	11%
cocktail simulation	14%–33%

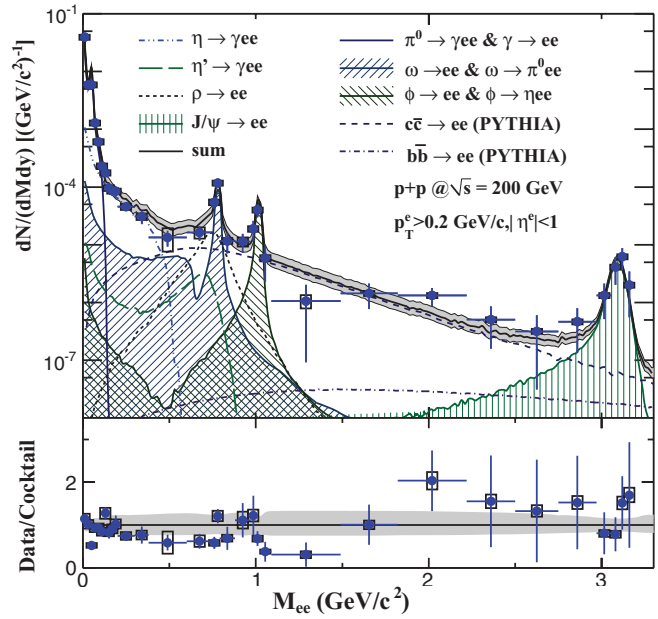

FIG. 12. (Color online) The comparison of the di-electron continuum between data and simulation after efficiency correction within the STAR acceptance in $\sqrt{s} = 200$ GeV NSD $p+p$ collisions. The di-electron continuum from simulations with different source contributions is also shown. The statistical errors on the data are shown as bars, while the systematic uncertainties are shown as boxes. The 11% normalization uncertainty on the data is not shown. The band on top of the solid curve illustrates the systematic uncertainties on the cocktail simulation.

they are also consistent within uncertainties. We find that better agreement between the cocktail simulation and data can be achieved by applying an additional scale factor (56%) to the η Dalitz decay contribution. Further details on this decay can be found in Sec. VI.

V. VECTOR MESON PRODUCTION

The yields of the ω, ϕ, and J/ψ long-lived vector mesons can be extracted from the di-electron continuum. We use the mixed-event technique to reconstruct the combinatorial background beneath the respective peaks. The mixed-event distribution is normalized by a constant to match the like-sign distribution in the mass region of 0.4–1.5 GeV/c^2, as discussed in Sec. III B. The background is then subtracted to obtain the signal, which will still contain some residual background of di-electron pairs from other sources, as described in Sec. IV A.

A two-component fit is used to extract the raw signal $\omega \to e^+e^-$ from the residual background in the invariant-mass range of $0.7 < M_{ee} < 0.85$ GeV/c^2. The first component represents the line shape (the $\omega \to e^+e^-$ signal shape); the second gives the residual background. The line shape of the $\omega \to e^+e^-$ invariant-mass distribution and the shape and magnitude of the background are determined from the simulations described in Sec. IV A. The systematic uncertainties of the $\omega \to e^+e^-$ raw yields are derived by changing the magnitude of the background allowed by the uncertainties of the cocktail

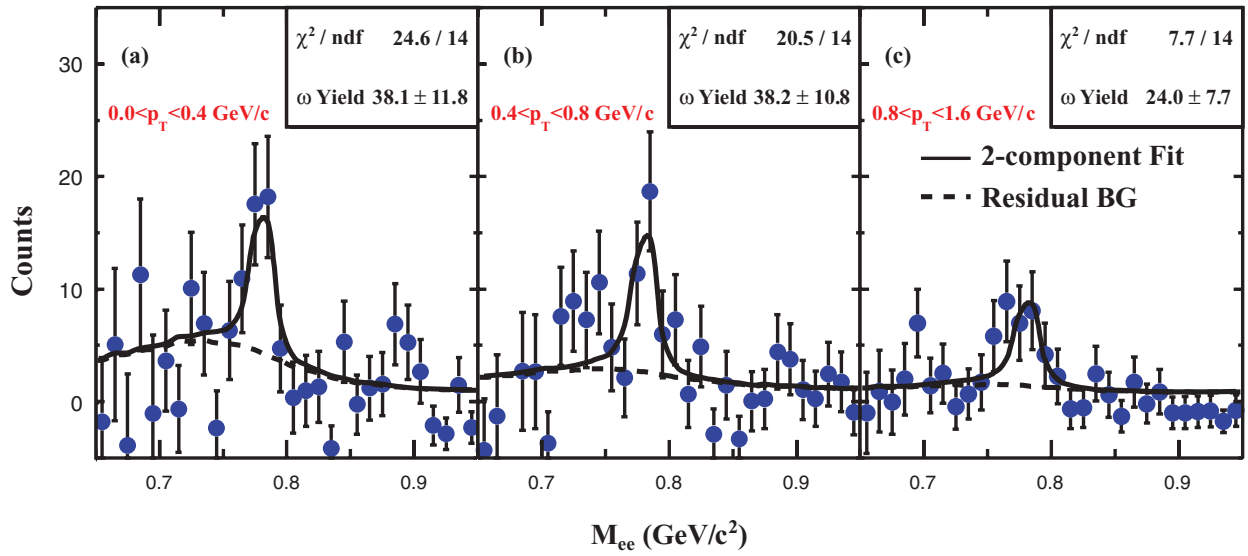

FIG. 13. (Color online) The M_{ee} distribution in the range $0.65 < M_{ee} < 0.95$ GeV/c^2 for three different p_T bins after the mixed-event background subtraction in $p + p$ collisions at $\sqrt{s} = 200$ GeV. The curves represent fits in the range $0.7 < M_{ee} < 0.85$ GeV/c^2 as described in the text. Errors on data points are statistical.

simulation and the analysis cuts. The total contribution to the raw yield is about 20%. Figure 13 shows the fit to the M_{ee} distribution for $0.7 < M_{ee} < 0.85$ GeV/c^2 in three different p_T bins for $p + p$ collisions at $\sqrt{s} = 200$ GeV.

In order to present the final differential invariant cross section as a function of p_T, the raw vector meson yield ($\omega \to e^+e^-$) is corrected for acceptance and all detector effects which reduce the measured raw yield relative to the actual yield. The total efficiency correction for $\omega \to e^+e^-$ for $|y| < 1$ is shown in Fig. 14. We use the simulations described in Sec. IV A to determine this correction, which accounts for limits in TPC acceptance and inefficiencies in TPC tracking, limits in the TOF acceptance and response, and the rejection of signal due to the dE/dx cut. The invariant yield is defined as follows:

$$\frac{d^2N}{2\pi p_T dp_T dy} = \frac{N_{\text{raw}}\text{NORM}}{2\pi p_T dp_T dy N_{\text{event}} \epsilon \text{B.R.}}, \tag{9}$$

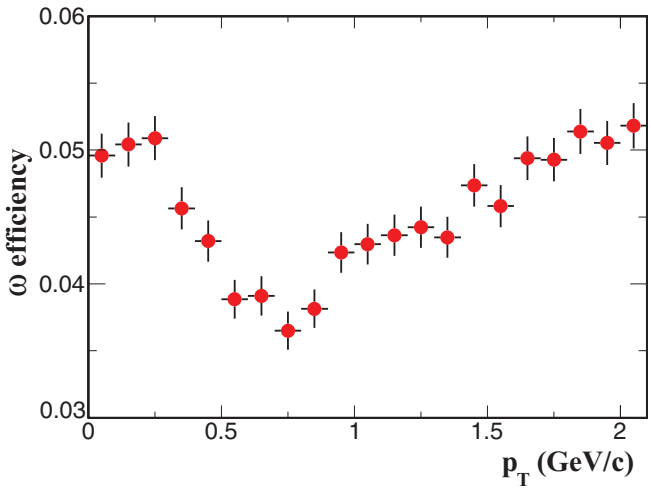

FIG. 14. (Color online) The efficiency including STAR acceptance for $\omega \to e^+e^-$ for $|y| < 1$ in $p + p$ collisions at $\sqrt{s} = 200$ GeV.

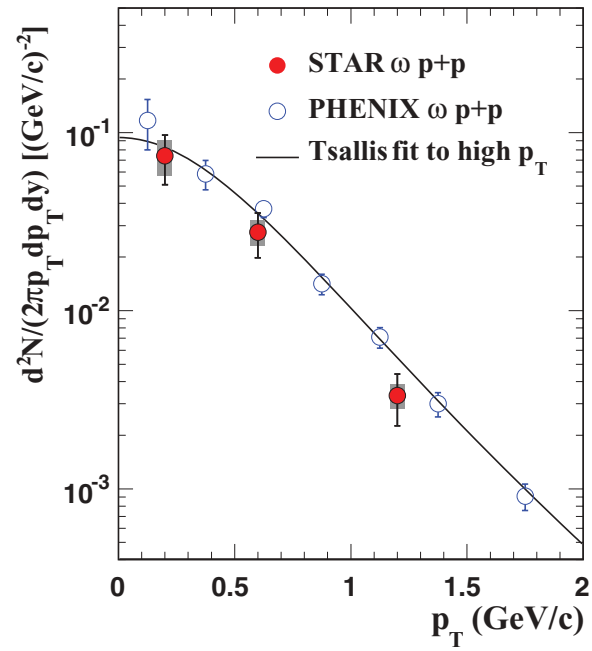

FIG. 15. (Color online) The $\omega \to e^+e^-$ invariant yield, divided by its B.R., in NSD $p + p$ collisions at $\sqrt{s} = 200$ GeV. The open circles represent PHENIX published results [49]. The bars are statistical errors and boxes are systematic uncertainties. A normalization uncertainty of 11% is not shown. The yields at the center of the p_T bin are corrected for finite bin width. The line represents the yields of ω from the Tsallis function fit to high-p_T ω yields measured from its hadronic decay and described in Sec. IV A.

TABLE III. Systematic uncertainties from different sources for ω yields.

Source	Contribution factors
two-component fit	9%–16%
$n\sigma_e$ cut	3%–7%
efficiency	10%
total normalization	11%

TABLE IV. Systematic uncertainties from different sources for ϕ and J/ψ dN/dy.

Source	Contribution factors	
	for ϕ	for J/ψ
two-component fit	10%	7%
$n\sigma_e$ cut	8%	27%
efficiency	10%	10%
total normalization	11%	11%

where $N_{\rm raw}$ represents the raw signal counts, $N_{\rm event}$ is the total event number, ϵ is the total efficiency and acceptance correction factor, B.R. is the branching ratio for $\omega \to e^+e^-$, and NORM is the normalization factor [$64 \pm 5\%$ for VPD triggered minimum-bias events taking into account the trigger bias and vertex finding efficiency determined by (and corrected) using PYTHIA simulations]. The ω invariant yield in NSD $p+p$ collisions at $\sqrt{s} = 200$ GeV is presented in Fig. 15. The systematic uncertainties are dominated by uncertainties in the two-component fit and uncertainties in total efficiency which are also described in Sec. IV A. Table III lists the detailed systematic uncertainties for ω yields from different sources. Our ω yields from di-electron decays are consistent with previous results [49] and with a prediction from a Tsallis fit, which fits spectra of other particles and high-p_T ω yields [31,44]. We obtain a mid-rapidity dN/dy of 0.10 ± 0.02 (stat.) $\pm$ 0.02 (sys.) for the ω.

In addition to $\omega \to e^+e^-$ yields, we also obtain the mid-rapidity yields, dN/dy, for the ϕ and J/ψ particles in NSD $p+p$ collisions at $\sqrt{s} = 200$ GeV. Due to limited statistics for each particle, the invariant-mass signal can only be extracted over all p_T, rather than individual bins. As before, we use a two-component fit in the region of M_{ee} for $0.98 < M_{ee} < 1.04$ GeV/c^2 for the $\phi \to e^+e^-$ and $3 < M_{ee} < 3.16$ GeV/c^2 for $J/\psi \to e^+e^-$. The line shapes of $\phi \to e^+e^-$ and $J/\psi \to e^+e^-$ are from simulations as discussed in Sec. IV A. The residual background shape and magnitude are obtained from the cocktail simulation, shown in Sec. IV A. The systematic uncertainties of the ϕ and J/ψ dN/dy due to the residual background are evaluated by changing the magnitude of the background allowed by the uncertainties of the cocktail simulation. The total efficiency correction for each particle is evaluated in the same way as for the $\omega \to e^+e^-$ analysis. Since the correction depends on p_T, we calculate a weighted average using the predicted spectra from the previously mentioned Tsallis fit as p_T weights. The total efficiency and acceptance correction factors for ϕ and J/ψ are 4.4% and 3.4%, respectively. The systematic uncertainty on the total efficiency correction is estimated to be 10%. The normalization uncertainty is 11% in $p+p$ collisions. Table IV lists the detailed systematic uncertainties for the ϕ and J/ψ dN/dy from different sources. Figure 16 shows the fits to the M_{ee} distributions used to obtain the mid-rapidity yields dN/dy for ϕ and J/ψ in NSD $p+p$ collisions at $\sqrt{s} = 200$ GeV. The final yields in those fits are subject to the total efficiency correction. The dN/dy for ϕ is 0.010 ± 0.002 (stat.) $\pm$ 0.002 (syst.), consistent with the measurements from $\phi \to K^+K^-$ [42,50]. The dN/dy for J/ψ is [2.1 ± 0.7 (stat.) $\pm$ 0.7 (syst.)] $\times$ 10^{-5}, consistent with previous measurements [45,51].

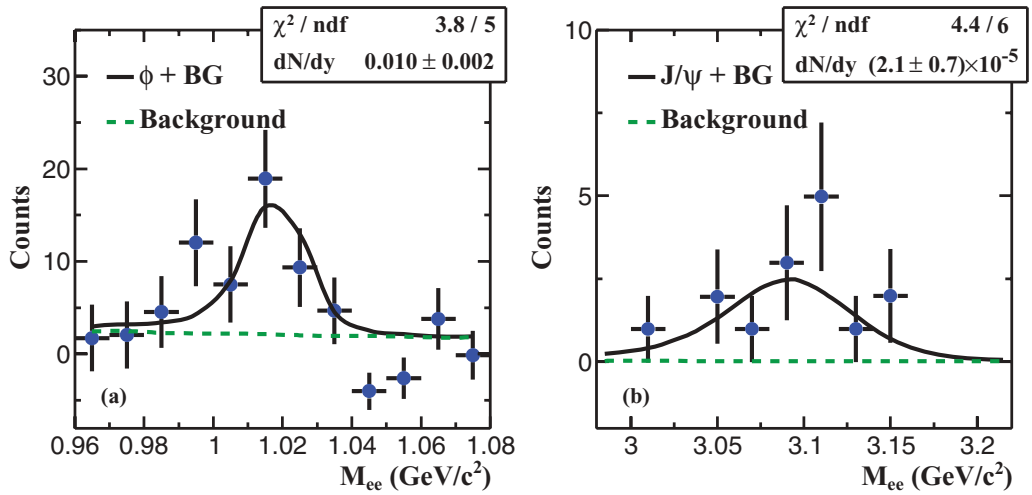

FIG. 16. (Color online) (a) The M_{ee} distribution after the mixed-event background subtraction for $0.96 < M_{ee} < 1.08$ GeV/c^2 in $p+p$ collisions at $\sqrt{s} = 200$ GeV. The curve represents the fit in the range of $0.98 < M_{ee} < 1.04$ GeV/c^2. Errors on data points are statistical. (b) The M_{ee} distribution after the mixed-event background subtraction for $2.98 < M_{ee} < 3.22$ GeV/c^2 in $p+p$ collisions at $\sqrt{s} = 200$ GeV. The curve represents the fit in the range of $3 < M_{ee} < 3.16$ GeV/c^2. There is no count in the unlike-sign and like-sign electron-pair distributions for $3.02 < M_{ee} < 3.04$ GeV/c^2 due to statistical fluctuations. Errors on data points are statistical.

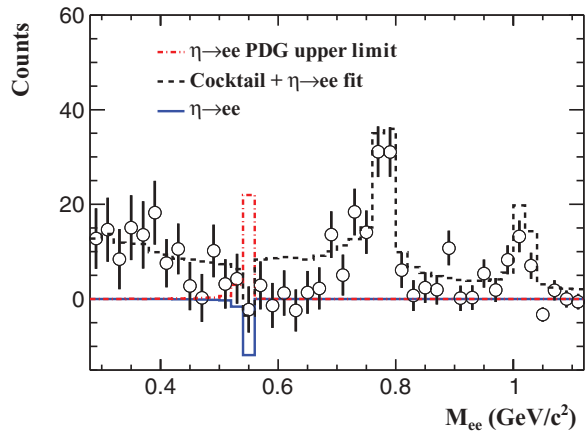

FIG. 17. (Color online) M_{ee} distribution for di-electron production in $p + p$ collisions at $\sqrt{s} = 200$ GeV. The dashed curve is the cocktail with the $\eta \to e^+e^-$ decay channel included in the fit. The $\eta \to e^+e^-$ contribution is shown as the solid curve. The dot-dashed peak is the $\eta \to e^+e^-$ contribution with the upper limit of its branching ratio from the Particle Data Group [52], which is 2.7×10^{-5}.

VI. THE RARE DECAY: $\eta \to e^+e^-$

As discussed in previous sections and shown in Fig. 12, the cocktail can describe the data reasonably well around the η mass without the $\eta \to e^+e^-$ decay channel. We zoom into the low-mass range and show the data and cocktail comparison in Fig. 17. The dot-dashed peak is the $\eta \to e^+e^-$ contribution with the upper limit of its B.R. from the Particle Data Group [36], which is 2.7×10^{-5} [52]. The dashed curve is a two-component fit with the $\eta \to e^+e^-$ decay channel included. The fit function is

$$AN_\eta + B \times \text{Cocktail}, \tag{10}$$

in which N_η is the expected η contribution with the line shape of $\eta \to e^+e^-$ after detector simulation, Cocktail is the expected cocktail contribution described in Sec. IV A without $\eta \to e^+e^-$, and A and B are fit parameters. A and B represent the B.R. for $\eta \to e^+e^-$ and a scale factor for the cocktail contribution, respectively. The solid curve shown in Fig. 17 represents the $\eta \to e^+e^-$ contribution from the fit. It gives the B.R. of $\eta \to e^+e^-$ to be $[-9.6 \pm 5.9\ (\text{stat.}) \pm 5.3\ (\text{syst.})] \times 10^{-6}$. The negative value of B.R. of $\eta \to e^+e^-$ is due to the statistical fluctuation at $M_{ee} = 0.55$ GeV/c^2. The systematic uncertainties are dominated by background subtraction (34%, the difference between mixed-event background subtraction and like-sign subtraction), electron purity (31%, determined by varying the $n\sigma_e$ cuts), and track quality cut (27%, determined by changing the cut of distance of closest approach between the track and the collision vertex).

In addition, although the Dalitz decay yield of $\eta \to \gamma e^+e^-$ is consistent with the cocktail expectation from the Tsallis fit to η measurements for $p_T > 2$ GeV/c described in Sec. IV A, the nominal value from the fit in Fig. 17 is about 56% of the input cocktail ($B = 56\%$). This additional factor leads to a better agreement between data and cocktail simulation compared to that shown in Fig. 12. This is equivalent to a smaller value of N_η and has to be taken into account when the upper limit at the 90% confidence level (CL) for the B.R. of $\eta \to e^+e^-$ is estimated.

With different background subtraction, electronic purity, and track quality cuts, we repeat the fit process described above to obtain the parameter A, the B.R. of $\eta \to e^+e^-$. The difference of the A values is attributed to the systematic uncertainties. In this fit procedure, we find that cut conditions do not contribute to the point-to-point variation around the η mass range and the statistical error of the parameter A remains unchanged. Therefore, the significance of an observable signal above the background only depends on the statistical fluctuation. To estimate the upper limit for the B.R. of $\eta \to e^+e^-$ at the 90% CL due to a possible statistical fluctuation, we utilize the statistical error 5.9×10^{-6} for the B.R. of $\eta \to e^+e^-$ from the fit and set the lower bound of the B.R. of $\eta \to e^+e^-$ to be zero instead of the negative value from the fit. The upper limit is found to be $5.9 \times 10^{-6} \times 1.65/0.56 = 1.7 \times 10^{-5}$, in which 1.65 is the upper endpoint of a confidence interval (the lower endpoint being zero) with a 90% CL for a standard normal distribution.

These results provide a promising first glimpse of a program for searching for rare decays of hadrons produced in relativistic heavy-ion collisions at STAR. With large hadron yields, high efficiency for electrons at low momentum, and high mass resolution, STAR provides a unique tool for such a program in the years to come.

VII. SUMMARY

The di-electron continuum is measured in $\sqrt{s} = 200$ GeV non-singly diffractive $p + p$ collisions within the STAR acceptance. The cocktail simulations are consistent with the data and provide a reference for future heavy-ion studies. The ω invariant yields are consistent with the results of previous publications. The dN/dy for ϕ and J/ψ are 0.010 ± 0.002 (stat.) ± 0.002 (syst.) and $[2.1 \pm 0.7\ (\text{stat.}) \pm 0.7\ (\text{syst.})] \times 10^{-5}$, respectively. These results are consistent with the previous measurements from $\phi \to K^+K^-$ and $J/\psi \to e^+e^-$. Our measurement lowers the current world limit of the branching ratio of $\eta \to e^+e^-$ from 2.7×10^{-5} to 1.7×10^{-5}.

ACKNOWLEDGMENTS

We thank the RHIC Operations Group and RCF at BNL, the NERSC Center at LBNL, and the Open Science Grid consortium for providing resources and support. This work was supported in part by the Offices of Nuclear Physics and High Energy Physics within the US Department of Energy Office of Science, the US NSF, the Sloan Foundation, the DFG cluster of excellence "Origin and Structure of the Universe" of Germany, CNRS/IN2P3, FAPESP CNPq of Brazil, the Ministry of Education and Science of the Russian Federation, NNSFC, CAS, MoST, and MoE of China, GA and MSMT of the Czech Republic, FOM and NWO of the Netherlands, DAE, DST, and CSIR of India, the Polish Ministry of Science and Higher Education, Korea Research Foundation, Ministry of Science, Education and Sports of the Republic of Croatia, and RosAtom of Russia.

[1] J. Adams *et al.*, Nucl. Phys. A **757**, 102 (2005).
[2] I. Arsene *et al.*, Nucl. Phys. A **757**, 1 (2005); K. Adcox *et al.*, *ibid.* **757**, 184 (2005); B. B. Back *et al.*, *ibid.* **757**, 28 (2005).
[3] R. Rapp and J. Wambach, Adv. Nucl. Phys. **25**, 1 (2000).
[4] G. David, R. Rapp, and Z. Xu, Phys. Rep. **462**, 176 (2008).
[5] G. Agakichiev *et al.*, Eur. Phys. J. C **41**, 475 (2005).
[6] R. Arnaldi *et al.*, Phys. Rev. Lett. **96**, 162302 (2006).
[7] R. Rapp and J. Wambach, Eur. Phys. J. A **6**, 415 (1999).
[8] G. E. Brown and M. Rho, Phys. Rep. **269**, 333 (1996).
[9] A. Adare *et al.*, Phys. Rev. C **81**, 034911 (2010).
[10] R. Rapp, J. Wambach, and H. van Hees, arXiv:0901.3289; H. van Hees and R. Rapp, Nucl. Phys. A **806**, 339 (2008).
[11] A. Adare *et al.*, Phys. Rev. Lett. **104**, 132301 (2010).
[12] T. Matsui and H. Satz, Phys. Lett. B **178**, 416 (1986); H. Satz, J. Phys. G **32**, R25 (2006); A. Mocsy and P. Petreczky, Phys. Rev. Lett. **99**, 211602 (2007); Y. Burnier, M. Laine, and M. Vepsalainen, J. High Energy Phys. 01 (2008) 043.
[13] A. E. Dorokhov, Phys. Part. Nucl. Lett. **7**, 229 (2010).
[14] J. D. Bjorken, R. Essig, P. Schuster, and N. Toro, Phys. Rev. D **80**, 075018 (2009).
[15] M. J. Savage, M. E. Luke, and M. B. Wise, Phys. Lett. B **291**, 481 (1992).
[16] L. Bergstrom, Z. Phys. C **14**, 129 (1982); L. Bergstrom *et al.*, *ibid.* **37**, 281 (1988).
[17] L. G. Landsberg, Phys. Rep. **128**, 301 (1985).
[18] B. Bonner *et al.*, Nucl. Instrum. Methods A **508**, 181 (2003); M. Shao *et al.*, *ibid.* **492**, 344 (2002); J. Wu *et al.*, *ibid.* **538**, 243 (2005).
[19] J. M. Landgraf *et al.*, Nucl. Instrum. Methods A **499**, 762 (2003).
[20] K. H. Ackermann *et al.*, Nucl. Instrum. Methods A **499**, 624 (2003).
[21] M. Anderson *et al.*, Nucl. Instrum. Methods A **499**, 659 (2003).
[22] H. Bichsel, Nucl. Instrum. Methods A **562**, 154 (2006).
[23] Y. Xu *et al.*, Nucl. Instrum. Methods A **614**, 28 (2010).
[24] M. Shao *et al.*, Nucl. Instrum. Methods A **558**, 419 (2006).
[25] J. Adams *et al.*, Phys. Lett. B **616**, 8 (2005); L. Ruan, Ph.D. thesis, University of Science and Technology of China, 2005, arXiv:nucl-ex/0503018.
[26] W.J. Llope *et al.*, Nucl. Instrum. Methods A **522**, 252 (2004).
[27] J. Adams *et al.*, Phys. Rev. Lett. **91**, 172302 (2003).
[28] B. I. Abelev *et al.*, Phys. Rev. C **79**, 034909 (2009).
[29] J. Adams *et al.*, Phys. Rev. Lett. **94**, 062301 (2005).
[30] L. Ruan *et al.*, Nucl. Phys. A **855**, 269 (2011); B. Huang, Ph.D. thesis, University of Science and Technology of China, 2011.
[31] Z. Tang, Y. Xu, L. Ruan, G. Van Buren, F. Wang, and Z. Xu, Phys. Rev. C **79**, 051901 (2009); M. Shao *et al.*, J. Phys. G **37**, 085104 (2010).
[32] C. Adler *et al.*, Phys. Rev. Lett. **87**, 262302 (2001); J. Adams *et al.*, *ibid.* **92**, 112301 (2004).
[33] N. M. Kroll and W. Wada, Phys. Rev. **98**, 1355 (1955).
[34] R. Rapp, Nucl. Phys. A **725**, 254 (2003); E. V. Shuryak and G. E. Brown, *ibid.* **717**, 322 (2003); P. F. Kolb and M. Prakash, Phys. Rev. C **67**, 044902 (2003).
[35] J. Adams *et al.*, Phys. Rev. Lett. **92**, 092301 (2004).
[36] K. Nakamura *et al.*, J. Phys. G **37**, 075021 (2010).
[37] R. Arnaldi *et al.*, Phys. Lett. B **677**, 260 (2009).
[38] M. N. Achasov *et al.*, Phys. Lett. B **504**, 275 (2001).
[39] The branching ratio of $\eta' \to \gamma e^+ e^-$, 4.7×10^{-4}, is determined by the B.R. of $\eta' \to \gamma\gamma$ and the ratio of the B.R. of $\eta' \to \gamma e^+ e^-$ to the B.R. of $\eta' \to \gamma\gamma$ [17].
[40] H. Alvensleben *et al.*, Nucl. Phys. B **25**, 333 (1971).
[41] J. Adams *et al.*, Phys. Lett. B **637**, 161 (2006).
[42] J. Adams *et al.*, Phys. Lett. B **612**, 181 (2005).
[43] S. S. Adler *et al.*, Phys. Rev. C **75**, 024909 (2007).
[44] S. S. Adler *et al.*, Phys. Rev. C **75**, 051902 (2007).
[45] A. Adare *et al.*, Phys. Rev. Lett. **98**, 232002 (2007).
[46] H. Agakishiev *et al.*, Phys. Rev. D **83**, 052006 (2011).
[47] T. Sjöstrand *et al.*, Comput. Phys. Commun. **135**, 238 (2001).
[48] A. Adare *et al.*, Phys. Rev. Lett. **97**, 252002 (2006).
[49] A. Adare *et al.*, Phys. Rev. D **83**, 052004 (2011).
[50] A. Adare *et al.*, Phys. Rev. C **83**, 024909 (2011).
[51] B. I. Abelev *et al.*, Phys. Rev. C **80**, 041902 (2009).
[52] T. E. Browder *et al.*, Phys. Rev. D **56**, 5359 (1997); M. Berlowski *et al.*, *ibid.* **77**, 032004 (2008).